Supplementary Information

Materials and methods

Chemicals

All reagents are of analytical grade and can be used directly without further purification. Copper sulfate ($CuSO_4$), sodium sulfate (Na_2SO_4), potassium nitrate (KNO_3), potassium nitrite (KNO_2), sodium hydroxide (NaOH), n-(1-naphthalenyl)-ethylenediamine dihydrochloride ($C_{12}H_{14}N_2 \cdot 2HCl$), and ammonium chloride (NH_4Cl) were purchased from Sinopharm Chemical Reagent Co. Ltd. Hydrochloric acid (HCl), phosphoric acid (H_3PO_4), sulfamic acid (H_3NO_3S), and sulfanilamide ($C_6H_8N_2O_2S$) were purchased from Shanghai Macklin Reagent Co., Ltd (Shanghai, China). Sodium hypochlorite (NaClO), sodium citrate dihydrate ($C_6H_5Na_3O_7 \cdot 2H_2O$), sodium salicylate ($C_7H_5O_3Na$), and sodium nitroferricyanide dihydrate ($C_5FeN_6Na_2O \cdot 2H_2O$) were purchased from Tianjin Damao Chemical Reagent Factory (Tianjin, China). Nafion 115 membranes were purchased from Shanghai Hesen Electronics Co. Ltd (Shanghai, China). Carbon fiber paper (HCP020N) was purchased from Toray Limited (Japan). All solutions involved in the whole experiment were prepared using deionized water.

Catalyst characterization

The electrochemical workstation (CHI760E) was used to collect electrochemical signals on an H-type electrolytic cell equipped with a three-electrode system. The structural morphology of CP/CuO_x was characterized using a light microscope (Olympus CX23) and a field emission scanning electron microscope (FE-SEM, Zeiss Supra 40). The conductivity of the electrolyte solution was detected using a conductivity meter (STARTER 300C). Raman spectra were recorded on the Raman

spectrometer (LABRAM HR800) under the excitation of a 532 nm laser. X-ray diffraction (XRD, Miniflex600) was also performed using a Bruker-D8 instrument, and Cu Kα radiation (λ = 0.15418 nm), and an X-ray photoelectron spectrometer (XPS, ESCALAB 250) was used to investigate the elemental composition.

Pretreatment of the Carbon Fiber Paper (CP)

First, carbon fiber paper pieces (1.0 cm x 2.0 cm) were cleaned by immersion in 30 mL of anhydrous ethanol for 10 min using ultrasonic cleaning to remove surface oils and contaminants. After rinsing five times with deionized water, they were dried at 60°C. Next, the papers were treated with 1 M hydrochloric acid solution for 10 min using ultrasound to remove the oxide layer. After five rinses with deionized water, they were dried again at 60°C for later use.

Determination of NO_3^-, NO_2^-, NH_4^+, N_2H_2, H_2 and N_2

The concentration of NO_3^- in the electrolyte was monitored by a colorimetric method.[1] KNO_3 solutions were prepared in gradients of 100, 80, 60, 40, 20 and 0 μM. The electrolyte was diluted to the test concentration range. For 5.0 mL of the test solution, 0.1 mL of 0.1 M HCl solution, and 0.01 mL of 0.8 wt.% H_3NO_3S solution was added. After standing for 10 min at room temperature, UV-Vis method was used. Spectra were collected from 200-280 nm and absorption intensities at 220 nm and 275 nm were recorded for NO_3^- calculation (Fig. S1).

The Griess method was used to determine NO_2^- in the electrolyte.[2] KNO_2 solutions were prepared at concentrations of 2, 1, 0.8, 0.6, 0.4, 0.2 and 0 μg mL^{-1}. A color developer was prepared, and 0.1 mL was added to 5.0 mL of the test solution and allowed to stand for 20 min before testing. UV-Vis spectra at 400-650 nm were collected and the absorbance at 540 nm was recorded for NO_2^- concentration (Fig. S2).

Ammonia was detected by the indophenol blue colorimetry.[3] NH_4Cl solutions with concentrations of 10, 7, 5, 3, 1, 0.5 and 0 μg mL^{-1} were prepared. A mixture was kept at 25 °C for 2 hours and the absorbance of the colorimetric solution was recorded at 655 nm. The UV-visible absorbance at 655 nm was determined from the full wave spectrum at 500-850 nm (Fig. S3). During sampling, the electrolyte was diluted 20 times and the ammonia concentration was determined by interpolation from the standard curve based on the absorbance at 655 nm.

N_2H_4 in the electrolyte was measured by the Watt and Chrisp method in a UV-visible spectroscopy. Spectra were recorded in the wavelength range of 400-550 nm. The absorbance at 455 nm was then used for calibration. The relationship between calibration concentration and absorbance was obtained using standard hydrazine hydrate at different concentrations (1.0, 0.8, 0.6, 0.4 and 0.2 μg/mL).

H_2 and N_2 were detected using a Shimadzu GC-2014 gas chromatograph. The chromatograph was equipped with flame ionization detectors and a thermal conductivity detector (TCD), of which the TCD can be used for the detection of H_2 and N_2.

Theoretical calculations

The Vienna Ab initio Simulation Package (VASP) was used to perform all density functional theory (DFT) calculations within the generalized gradient approximation (GGA) using the Perdew-Burke-Ernzerhof (PBE) functional. The projected augmented wave (PAW) potentials to describe the ionic cores and take valence electrons into account using a plane wave basis set with a kinetic energy cutoff of 400 eV have been chosen. Geometry optimizations were performed with the force convergency smaller than 0.05 eV/Å. All the atoms are relaxed in all the calculations, and the DFT-D3

empirical correction method was employed to describe the van der Waals interactions.

The Monkhorst-Pack k-points of 3×3×1 was chosen for all the calculations.

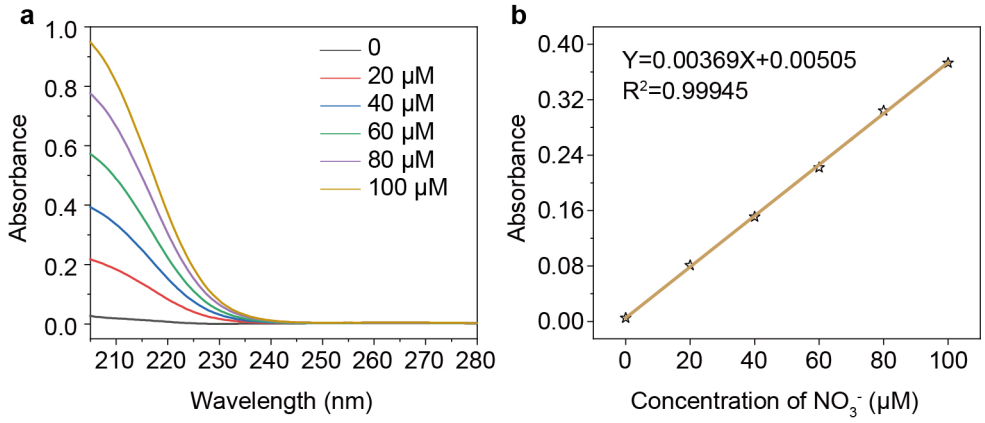

Figure S1. a) UV absorption spectra of a set of NO_3^- standard solution in alkaline conditions. b) The standard curve between NO_3^- concentration and its corresponding absorbance value summarized from in figure a.

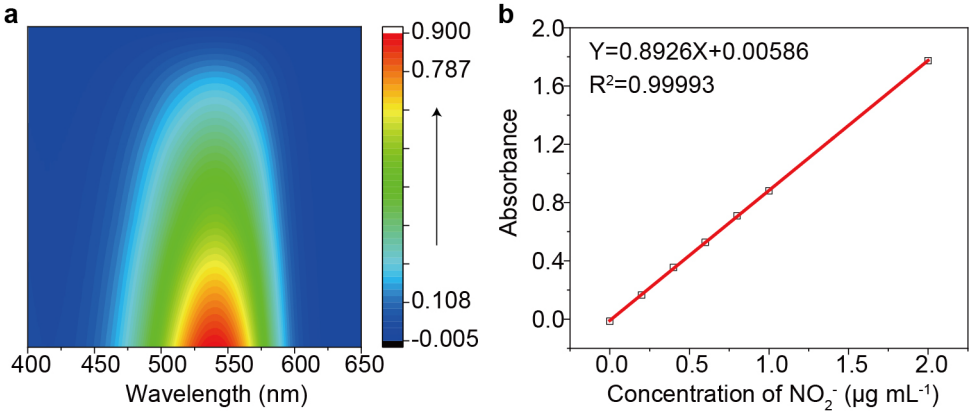

Figure S2. a) Three-dimension UV absorption spectra of a set of NO_2^- standard solution in alkaline conditions. b) The standard curve between NO_2^- concentration and its corresponding absorbance value summarized from in figure a.

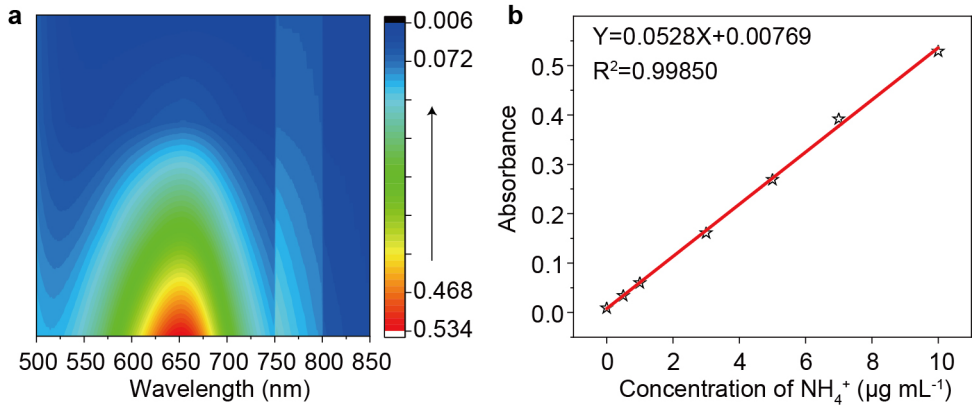

Figure S3. a) Three-dimension UV absorption spectra of a set of NH_4^+ standard solution in alkaline conditions. b) The standard curve between NH_4^+ concentration and its corresponding absorbance value summarized from in figure a.

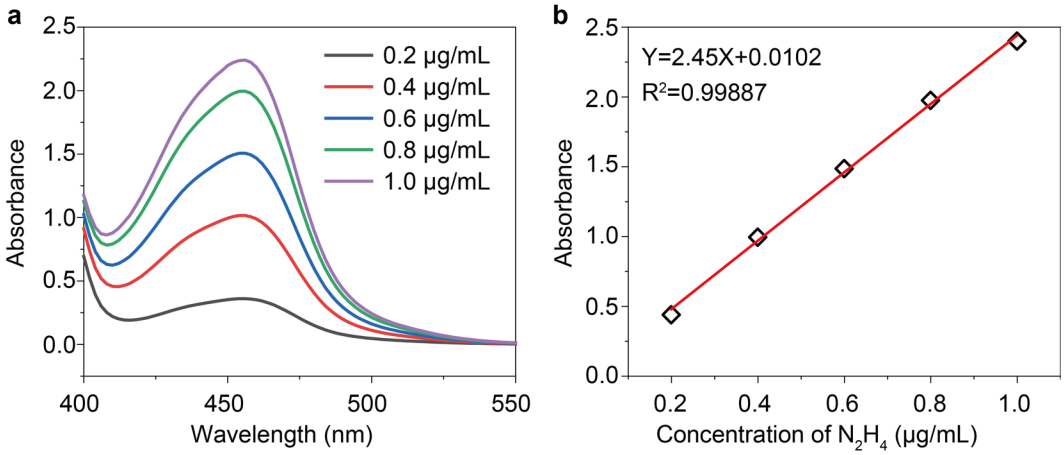

Figure S4. a) UV absorption spectra of a set of N_2H_4 standard solution in alkaline conditions. b) The standard curve between the pre-designed N_2H_4 concentration and its absorbance value.

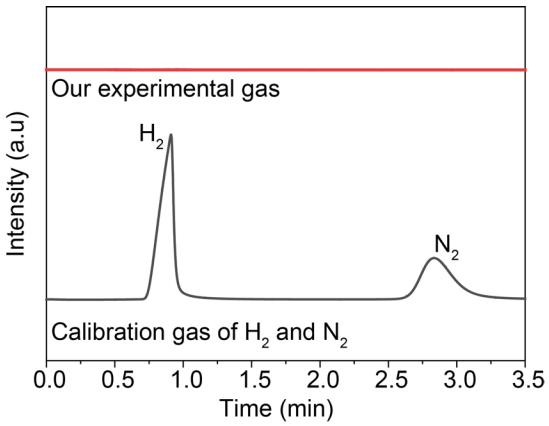

Figure S5. The collected gas products from CP/CuO_x-based electroreduction process at -1.0 V vs. RHE and the calibration gas of 10% H_2 and 75% N_2 detected by the gas chromatography apparatus.

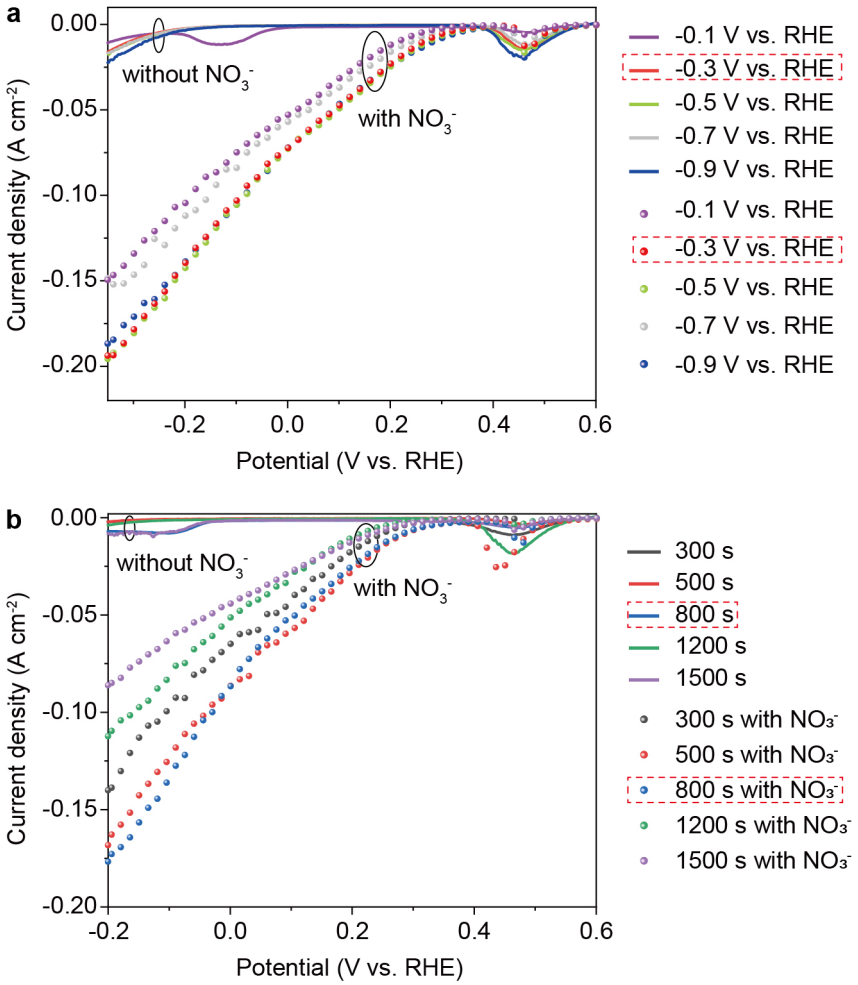

Figure S6. a) LSV curves of catalysts with different deposition potentials. b) LSV of the catalyst at 0.3 V vs. RHE with different deposition time.

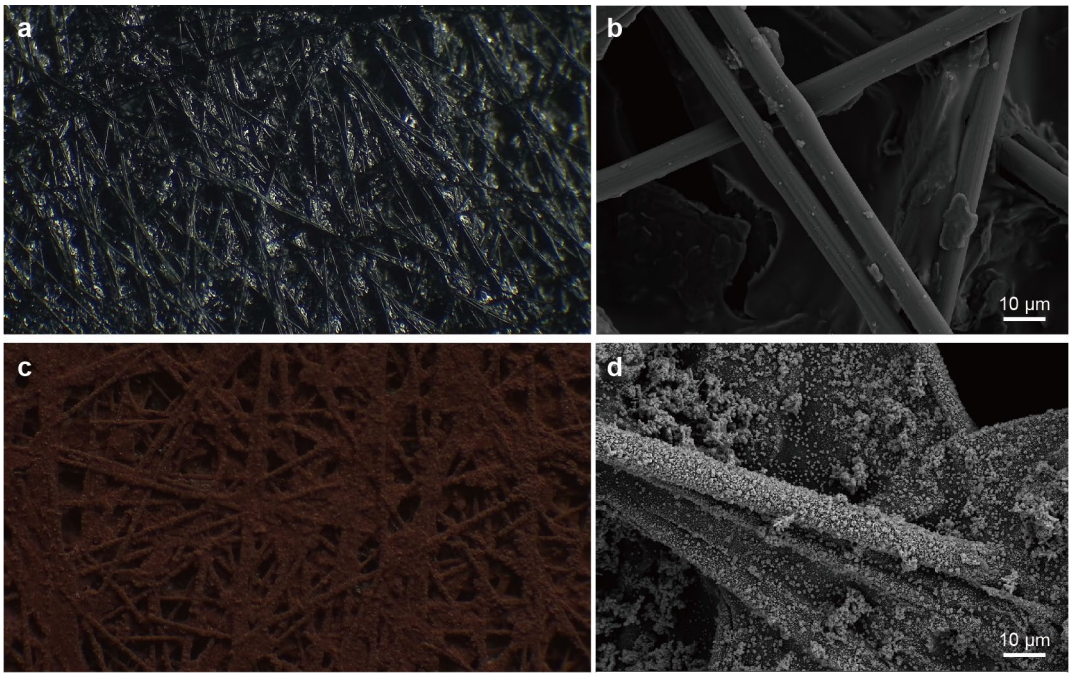

Figure S7. Optical microscope images of a) CP and c) CP/Cu, SEM images of b) CP and d) CP/Cu.

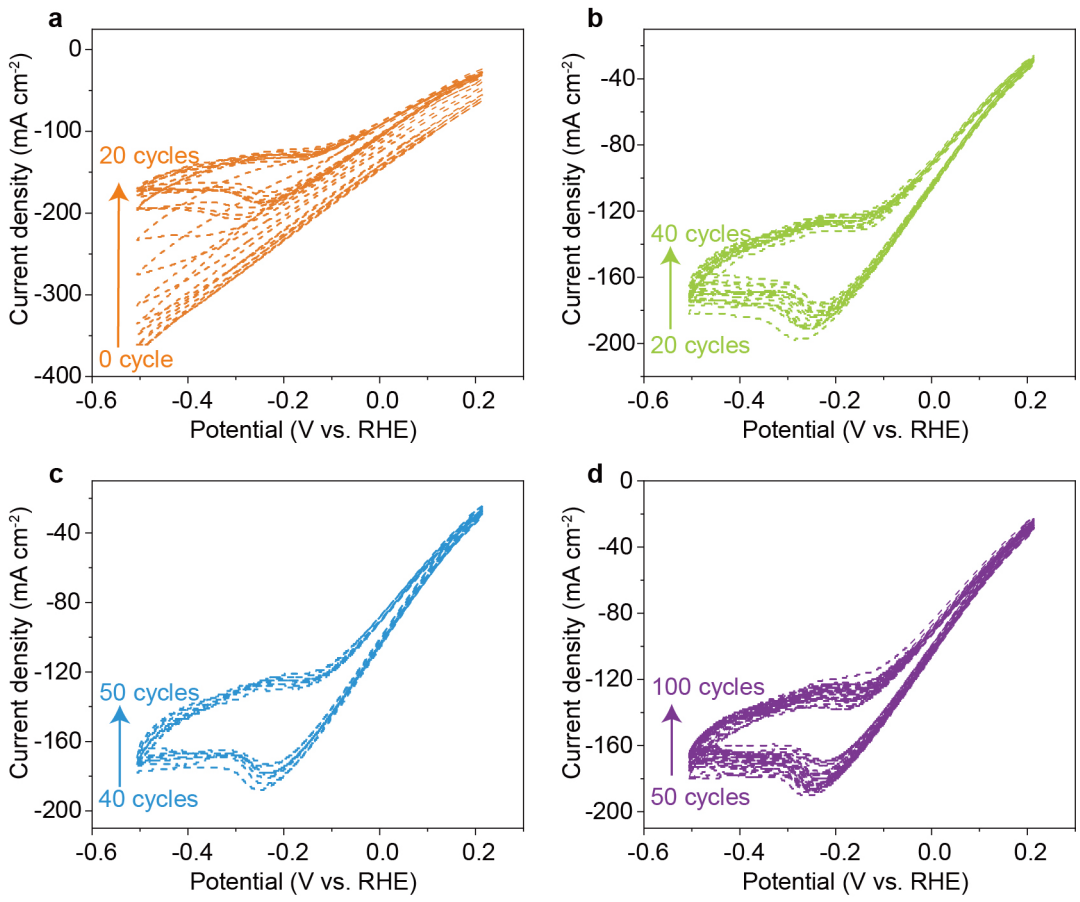

Figure S8. CV curve of CP/CuO_x a) 0 to 20 cycles, b) 20 to 40 cycles, c) 40 to 50 cycles and d) 50 to 100 cycles.

Table S1. Structure parameters of CP/CuO_x from the Rietveld refinement of XRD patterns

Items	CP/CuO_x	CP/CuO_{x+1}	CP/CuO_{x+2}	CP/CuO_{x+3}
a (Å)	4.26529	4.26787	4.26912	4.26853
b (Å)	4.26529	4.26787	4.26912	4.26853
c (Å)	4.26529	4.26787	4.26912	4.26853
α=β=γ	90°	90°	90°	90°
Unit cell volume (A^3)	77.6	77.7	77.8	77.8
ρ (g/cm^3)	6.1237	6.1126	6.1072	6.1098
μ (1/cm)	295.6	295.1	294.8	294.9

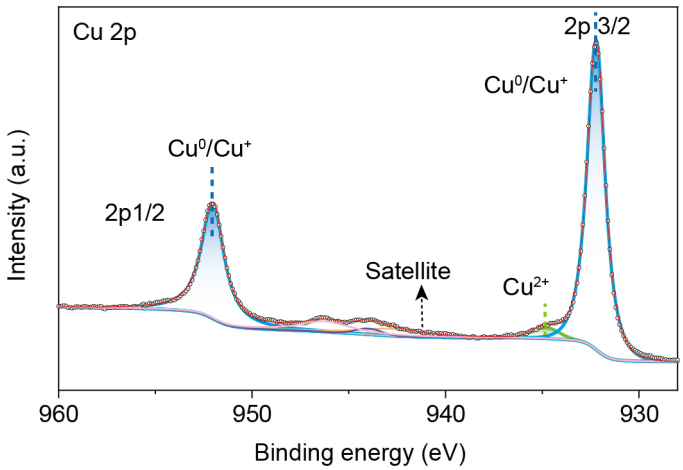

Figure S9. High-resolution Cu 2p XPS spectrum of CP/CuO_x.

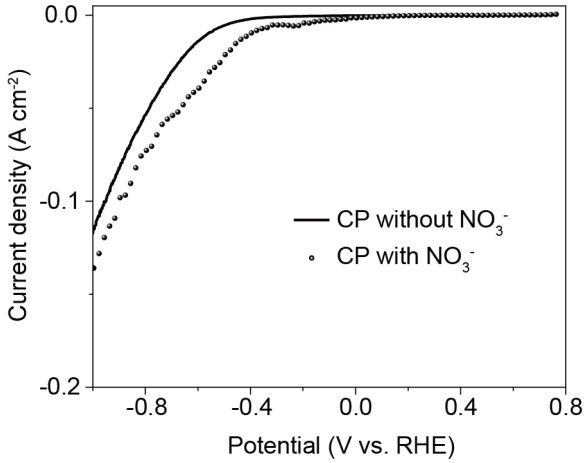

Figure S10. LSV of CP in Ar saturated 1 M KOH solution (pH = 13.8) with or without 0.1 M NO_3^-.

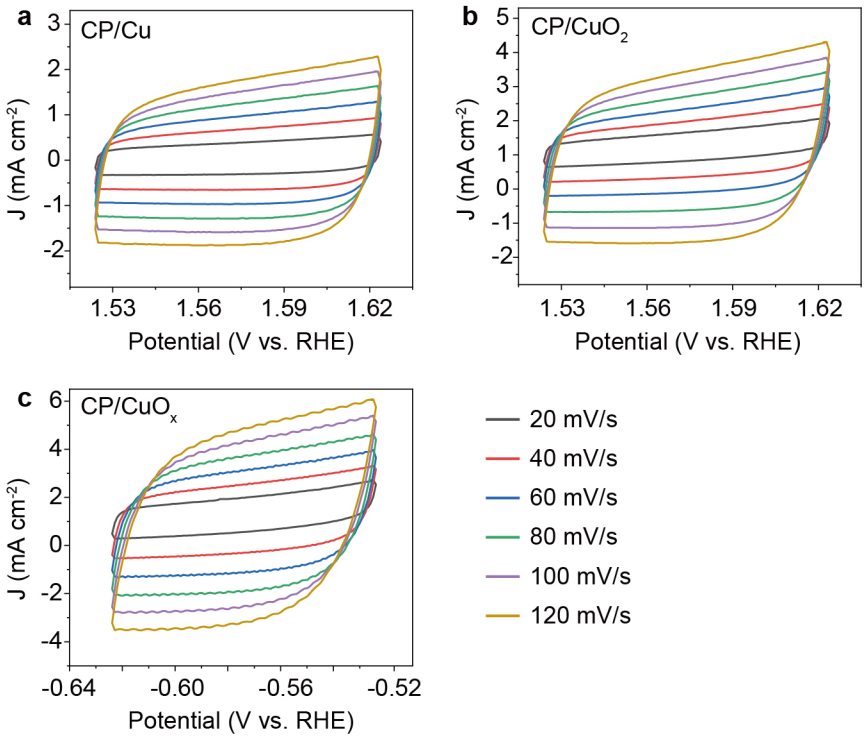

Figure S11. CV test of CP/Cu, CP/CuO_2 and CP/CuO_x in Ar saturated 1 M KOH solution (pH = 13.8).

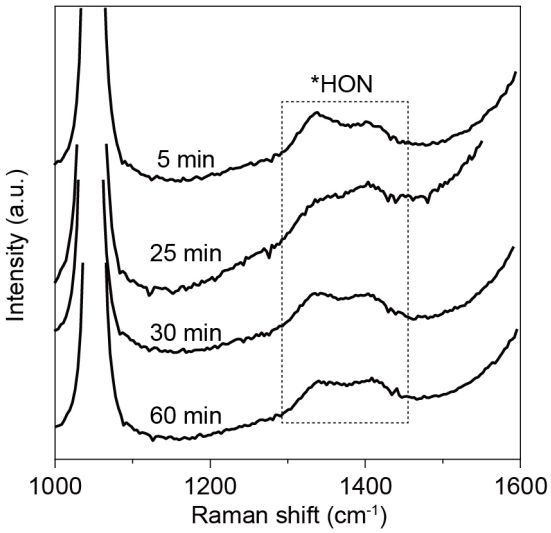

Figure S12. Enlarged image of Raman spectra from figure 2f in maintext to manifest the signal of *HON.

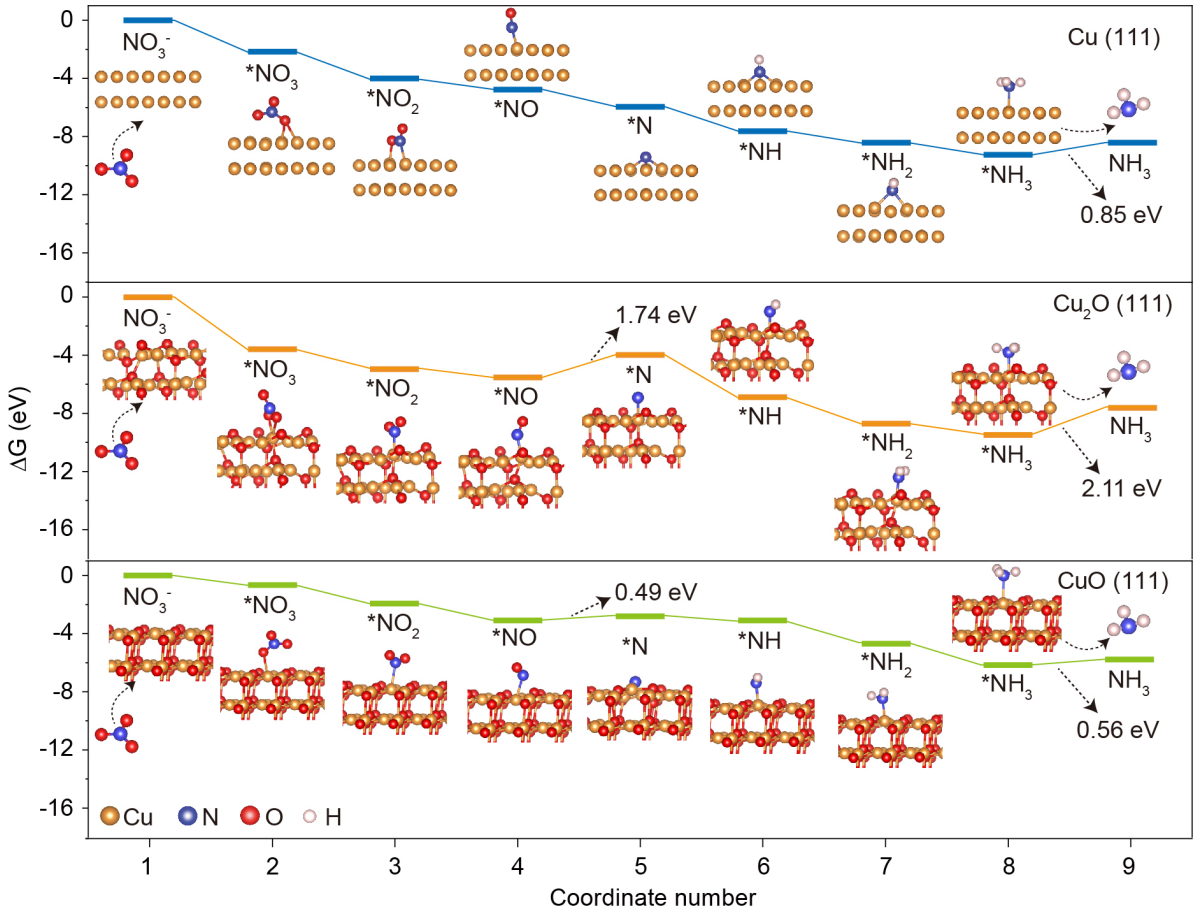

Figure S13. The Gibbs free energy diagram of nitrate reduction to ammonia on different copper interfaces.

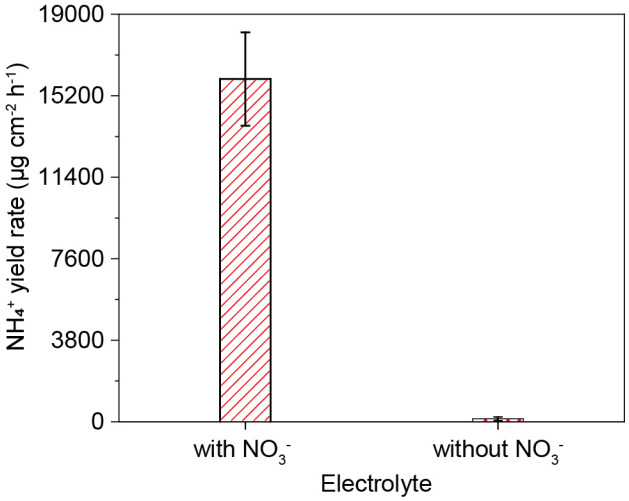

Figure S14. The comparison of NH_4^+ yield catalyzed by CP/CuO_x in NO_3^- solution with NO_3^- or without NO_3^-.

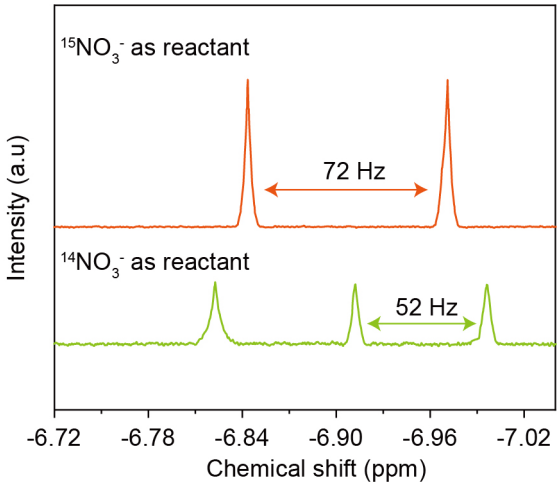

Figure S15. ^{1}H NMR spectra of electrolyte performed by CP/CuO_x using $^{14}NO_3^-$ or $^{15}NO_3^-$ as N-source.

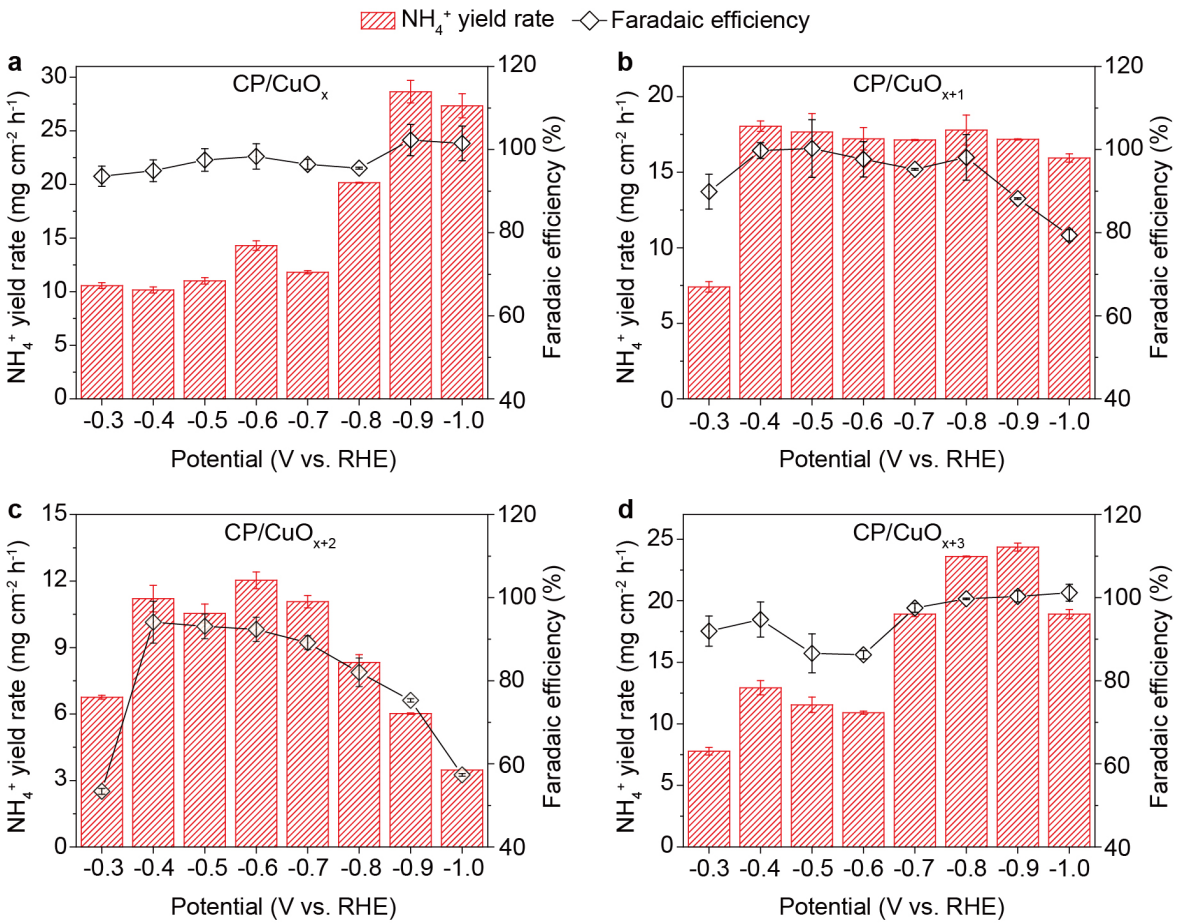

Figure S16. Faradaic efficiency and NH_4^+ yield at different step potentials of a) CP/CuO_x, b) CP/CuO_{x+1}, c) CP/CuO_{x+2} and d) CP/CuO_{x+3}.

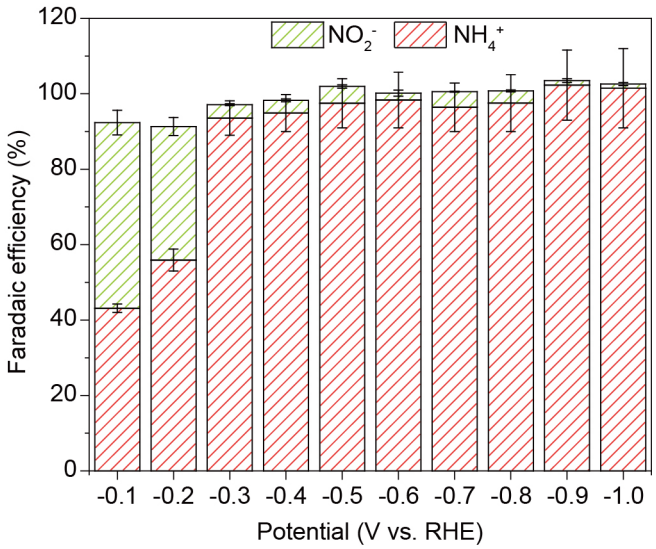

Figure S17. Faradaic efficiency of NH_4^+ and NO_2^- in CP/CuO_x-based electroreduction process.

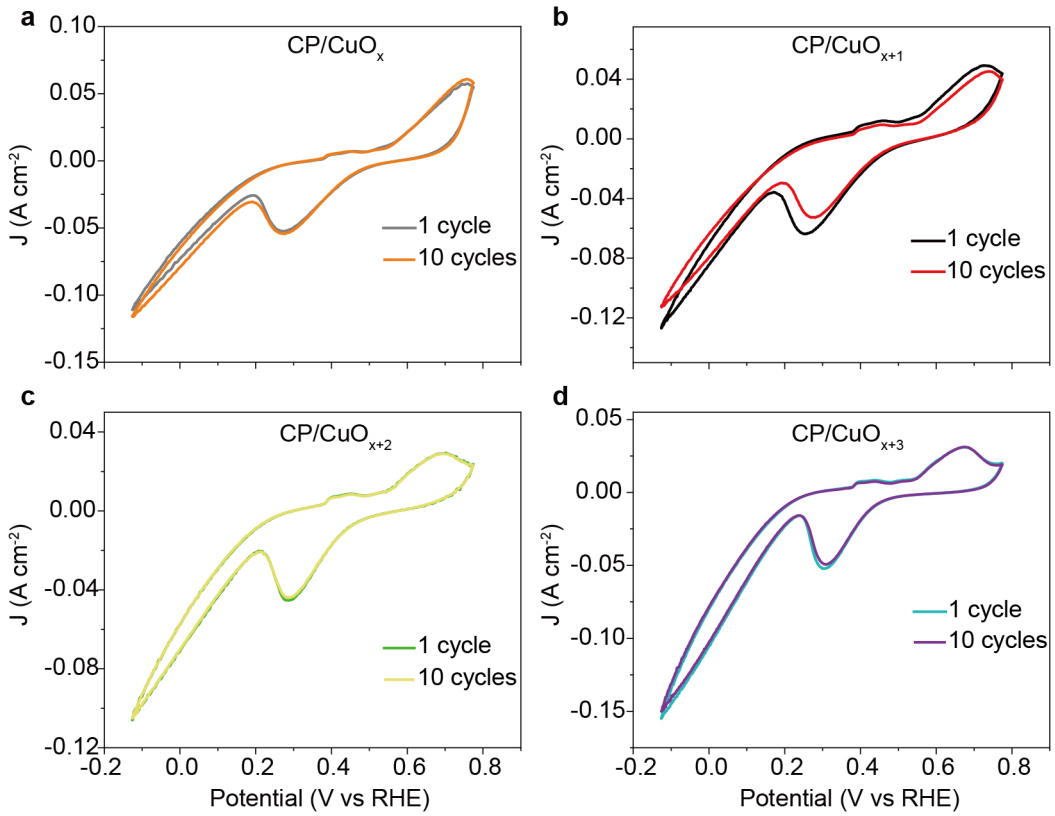

Figure S18. Faradaic efficiency and NH_4^+ yield at different step potentials of CV curve of a-d) CP/CuO_x, CP/CuO_{x+1}, CP/CuO_{x+2} and CP/CuO_{x+3}.

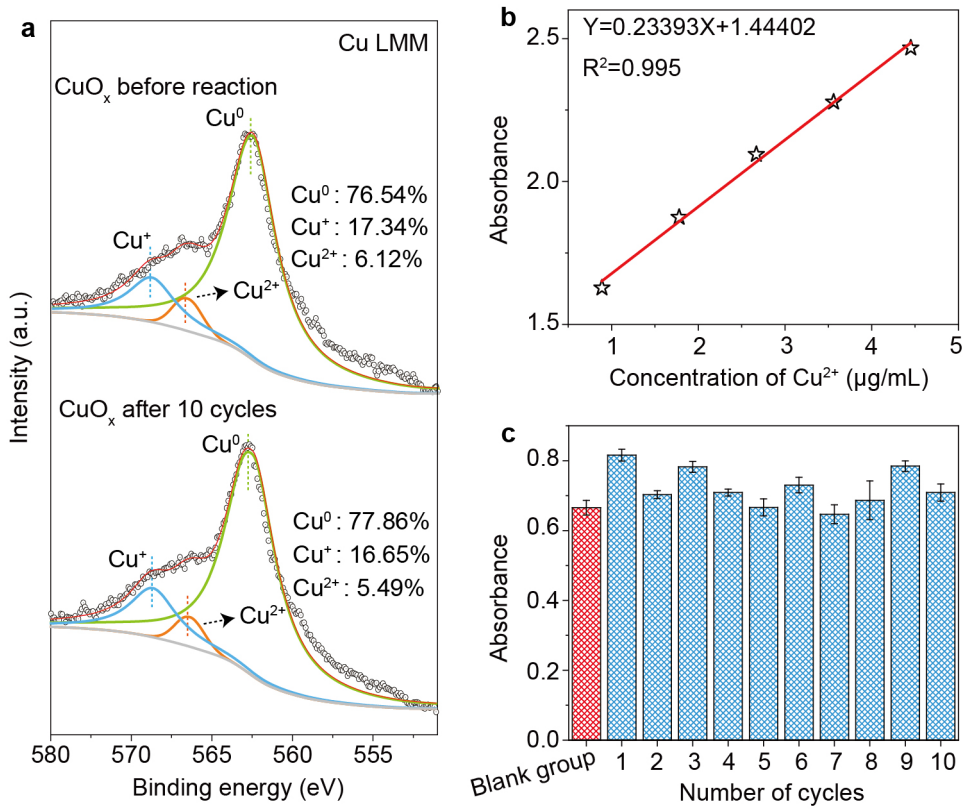

Figure S19. a) Cu LMM XPS spectra of CP/CuO_x before and after reaction. b) The standard curve between the pre-designed Cu^{2+} concentration and its absorbance value to be used for detection of copper leaching in electrolysis. $CuSO_4$ as the resource of Cu^{2+}. c) The measured atomic absorption value of copper ion in each cyclic test.

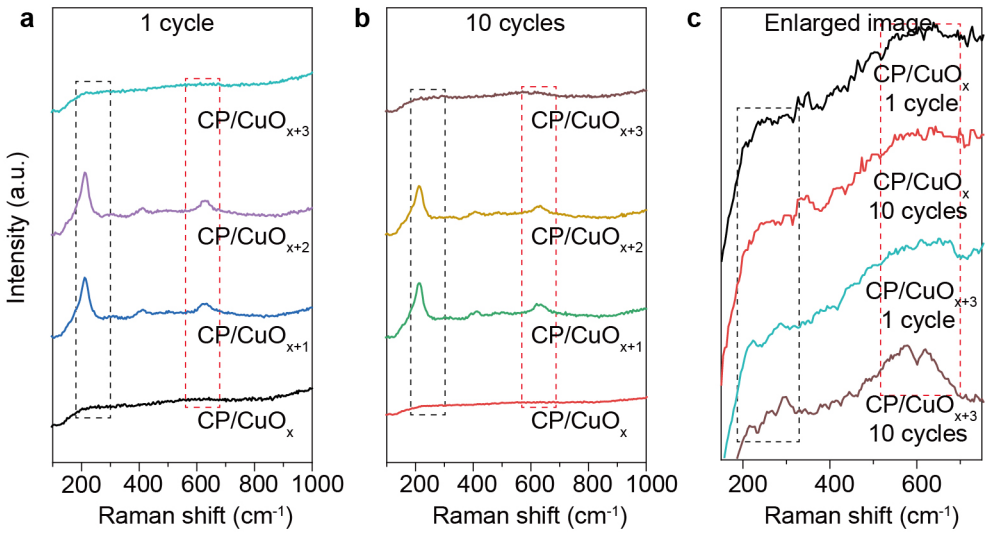

Figure S20. Raman spectra of CP/CuO_x series before and after reactions.

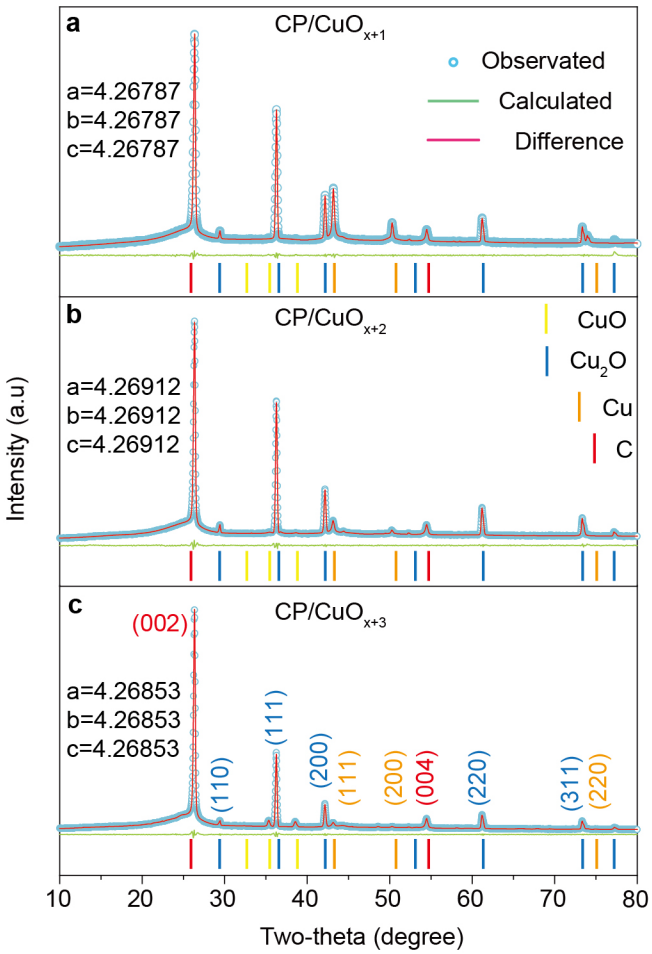

Figure S21. XRD patterns of a-c) CP/CuO$_{x+1}$, CP/CuO$_{x+2}$ and CP/CuO$_{x+3}$ (Cu_2O: JCPDF No. 05-0667; CuO: JCPDF No. 48-1548; Cu: JCPDF No. 04-0836; C: JCPDF No. 23-0064).

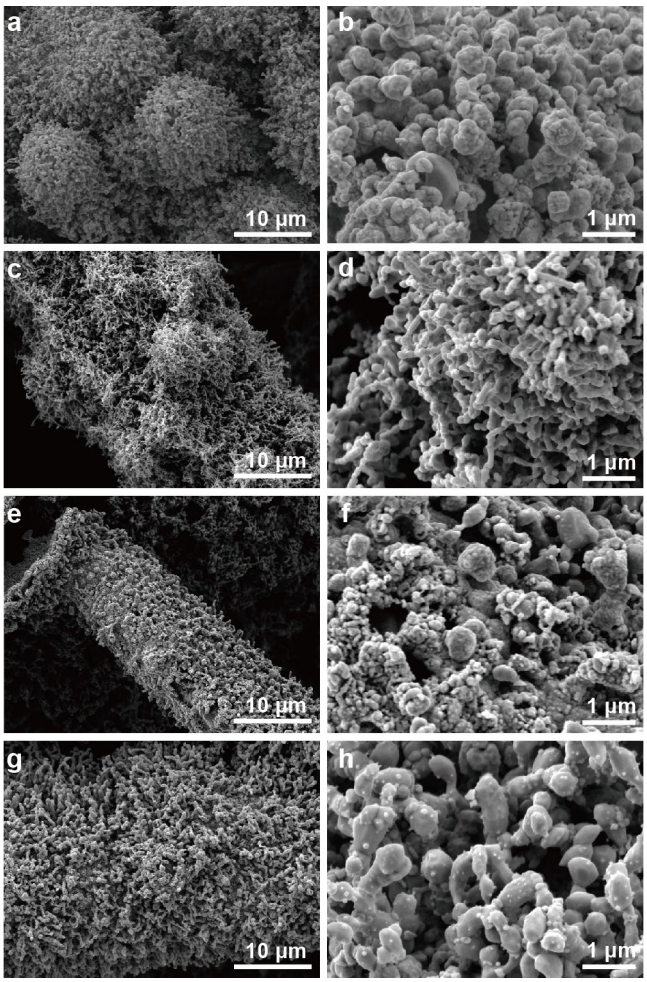

Figure S22. SEM images of a and b) CP/CuO_x, c and d) CP/CuO_{x+1}, e and f) CP/CuO_{x+2}, g and h) CP/CuO_{x+3}.

Table S2. Performance comparison of ammonia electrosynthesis and its Faradaic efficiency by NO_3RR between our work and the reported works

Catalysts	NH_4^+ yield rate (mg h^{-1} cm^{-2})	FE	Reference
CuO NWAs	4.16 @ -0.85 V	95.8% @ -0.85 V	4
CuCl-BEF	1.82 @ -1.0 V	44.7% @ -1.0 V	5
CoP/CC	0.32 @ -0.4 V	65% @ -0.4 V	6
Cu_3P NA/CF	0.848 @ -0.9 V	62.9% @ -0.6 V	7
Fe SAC	7.82 @ -0.85 V	75% @ -0.66 V	8
a-RuO_2	1.97 @ -0.35 V	97.46% @ -0.35 V	9
Fe_3O_4/SS	10.15 @ -0.5 V	91.5% @ -0.5 V	10
Cu-PTCDA	0.44 @ -0.4 V	85.9% @ -0.4 V	11
$MnCuO_x$-H	9.4 @ -0.63 V	86.4% @ -0.63 V	12
Rh@Cu	21.59 @ -0.2 V	93% @ -0.2 V	13
Strained Ru	19.9 @ -0.2 V	99% @ -0.2 V	14
CuO-Co_3O_4/Ti	1.65 @ -0.9 V	54.5% @ -0.9 V	15
Pd(111)	9.32 @ -0.7 V	79.91% @ -0.7 V	16

Table S3. Cu valence of CP/CuO_x, CP/CuO_{x+1}, CP/CuO_{x+2} and CP/CuO_{x+3}

Catalysts	Cu^0/Cu^+	Cu^{2+}
CP/CuO_x	93.06%	6.94%
CP/CuO_{x+1}	90.12%	9.88%
CP/CuO_{x+2}	85.2%	14.80%
CP/CuO_{x+3}	74.09%	25.91%

References

References

[1] X. Zhao, Z. Zhu, Y. N. He, H. B. Zhang, X. H. Zhou, W. B. Hu, M. Li, S. S. Zhang, Y. M. Dong, X. Hu, A. V. Kuklin, G. V. Baryshnikov, H. Ågren, T. Wågberg, G. Z. Hu, Simultaneous anchoring of Ni nanoparticles and single-atom Ni on BCN matrix promotes efficient conversion of nitrate in water into high-value-added ammonia, Chem. Eng. J., 2022, 433, 133190.

[2] Y. L. Liu, M. S. Chen, X. Zhao, H. R. Zhang, Y. Zhao, Y. T. Zhou, Unlocking the potential of sub-nanometer-scale copper via confinement engineering: A remarkable approach for electrochemical nitrate-to-ammonia conversion in wastewater treatment, Chem. Eng. J., 2023, 475, 146176.

[3] S. Z. Andersen, V. Colic, S. Yang, J. A. Schwalbe, A. C. Nielander, J. M. McEnaney, K. Enemark-Rasmussen, J. G. Baker, A. R. Singh, B. A. Rohr, M. J. Statt, S. J. Blair, S. Mezzavilla, J. Kibsgaard, P. C. K. Vesborg, M. Cargnello, S. F. Bent, T. F. Jaramillo, I. E. L. Stephens, J. K. Norskov, I. Chorkendorff, A rigorous electrochemical ammonia synthesis protocol with quantitative isotope measurements, Nature, 2019, 570, 504-508.

[4] Y. T. Wang, W. Zhou, R. R. Jia, Y. F. Yu, B. Zhang, Unveiling the activity origin of a copper-based electrocatalyst for selective nitrate reduction to ammonia, Angew. Chem. Int. Ed., 2020, 59, 5350-5354.

[5] W. J. Sun, H. Q. Ji, L. X. Li, H. Y. Zhang, Z. K. Wang, J. H. He, J. M. Lu, Built-in electric field triggered interfacial accumulation effect for efficient nitrate removal at ultra-low concentration and electroreduction to ammonia, Angew. Chem. Int. Ed., 2021,

60, 22933-22939.

[6] H. Zhang, G. Q. Wang, C. J. Wang, Y. L. Liu, Y. Yang, C. X. Wang, W. M. Jiang, L. M. Fu, J. Xu, CoP nanowires on carbon cloth for electrocatalytic NO_x^- reduction to ammonia, J. Electroanal. Chem., 2022, 910, 116171.

[7] J. Liang, B. Deng, Q. Liu, G. L. Wen, Q. Liu, T. S. Li, Y. L. Luo, A. A. Alshehri, K. A. Alzahrani, D. W. Ma, X. P. Sun, High-efficiency electrochemical nitrite reduction to ammonium using a Cu_3P nanowire array under ambient conditions, Green Chem., 2021, 23, 5487.

[8] Z. Y. Wu, M. Karamad, X. Yong, Q. Z. Huang, D. A. Cullen, P. Zhu, C. A. Xia, Q. F. Xiao, M. Shakouri, F. Y. Chen, J. Y. Kim, Y. Xia, K. Heck, Y. F. Hu, M. S. Wong, Q. L. Li, I. Gates, S. Siahrostami, H. T. Wang, Electrochemical ammonia synthesis via nitrate reduction on Fe single atom catalyst, Nat. Commun., 2021, 12, 2870.

[9] Y. T. Wang, H. J. Li, W. Zhou, X. Zhang, B. Zhang, Y. F. Yu, Structurally disordered RuO_2 nanosheets with rich oxygen vacancies for enhanced nitrate electroreduction to ammonia, Angew. Chem. Int. Ed., 2022, 61, e202202604.

[10] X. Y. Fan, L. S. Xie, J. Liang, Y. C. Ren, L. C. Zhang, L. C. Yue, T. S. Li, Y. L. Luo, N. Li, B. Tang, Y. Liu, S. Y. Gao, A. A. Alshehri, Q. Liu, Q. Q. Kong, X. P. Sun, In situ grown Fe_3O_4 particle on stainless steel: A highly efficient electrocatalyst for nitrate reduction to ammonia, Nano Res., 2022, 15, 3050-3055.

[11] G. F. Chen, Y. F. Yuan, H. F. Jiang, S. Y. Ren, L. X. Ding, L. Ma, T. P. Wu, J. Lu, H. H. Wang, Electrochemical reduction of nitrate to ammonia via direct eight-electron transfer using a copper-molecular solid catalyst, Nat. Energy., 2020, 5, 605-613.

[12] D. Jang, J. Maeng, J. Kim, H. Han, G. H. Park, J. Ha, D. Shin, Y. J. Hwang, W. B. Kim, Boosting electrocatalytic nitrate reduction reaction for ammonia synthesis by plasma-induced oxygen vacancies over $MnCuO_x$, Appl. Surf. Sci., 2023, 610, 155521.

[13] H. M. Liu, X. Y. Lang, C. Zhu, J. Timoshenko, M. Rüscher, L. C. Bai, N. Guijarro, H. B. Yin, Y. Peng, J. H. Li, Z. Liu, W. C. Wang, B. R. Cuenya, J. S. Luo, Efficient electrochemical nitrate reduction to ammonia with copper-supported rhodium cluster and single-atom catalysts, Angew. Chem. Int. Ed., 2022, 61, e202202556.

[14] J. Li, G. M. Zhan, J. H. Yang, F. J. Quan, C. L. Mao, Y. Liu, B. Wang, F. C. Lei, L. J. Li, A. W. M. Chan, L. P. Xu, Y. B. Shi, Y. Du, W. C. Hao, P. K. Wong, J. F. Wang, S. X. Dou, L. Z. Zhang, J. C. Yu, Efficient ammonia electrosynthesis from nitrate on strained ruthenium nanoclusters, J. Am. Chem. Soc., 2020, 142, 7036-7046.

[15] M. X. Yang, J. T. Wang, C. D. Shuang, A. M. Li, The improvement on total nitrogen removal in nitrate reduction by using a prepared $CuO\text{-}Co_3O_4$/Ti cathode, Chemosphere, 2020, 255, 126970.

[16] Y. Han, X. Y. Zhang, W. W. Cai, H. Zhao, Y. Y. Zhang, Y. Y. Sun, Z. Q. Hu, S. X. Li, J. P. Lai, L. Wang, Facet-controlled palladium nanocrystalline for enhanced nitrate reduction towards ammonia, J. Colloid Interface Sci., 2021, 600, 620-628.